Pergamon

Int. J. Heat Mass Transfer. Vol. 37, No. 6, pp. 967–976, 1994
Copyright © 1994 Elsevier Science Ltd
Printed in Great Britain. All rights reserved
0017-9310/94 $6.00+0.00

0017–9310(93)E0005–Z

Local heat transfer measurements from an elliptic jet impinging on a flat plate using liquid crystal

SANG-JOON LEE,† JUNG-HO LEE† and DAE-HEE LEE‡

†Advanced Fluids Engineering Research Center, Department of Mechanical Engineering,
Pohang Institute of Science and Technology, P.O. Box 125, Pohang, 790-600, Korea, ‡Department
of Mechanical Engineering, University of California, Berkeley, CA 94720, U.S.A.

(*Received* 23 *December* 1992 *and in final form* 5 *October* 1993)

Abstract—Local heat transfer measurements are reported for a turbulent submerged air jet issuing, normal to a heated flat plate, from an elliptical nozzle with an aspect ratio of 2.14. The Reynolds numbers used were 5000, 10 000, and 20 000 and the nozzle-to-plate distances were $L/D_e = 2, 4, 6$ and 10. The temperature on the heated plate surface was measured using a thermochromic liquid crystal and a digital image processing system that yielded an unbiased means for the quantitative color determination of the liquid crystal. The isothermal contour on the uniformly heated plate changed in shape from elliptic to near circle to elliptic again with an increasing nozzle-to-plate distance as the elliptical cross-section switched its orientation. For L/D_e from 4 to 10 and for all Reynolds numbers, the local Nusselt number decreased monotonically with increasing radial distance. However, for $L/D_e = 2$ and $Re = 10\,000$ and 20 000, the Nusselt number distributions exhibited second and third maxima. This may be attributed by the induced toroidal vorticities that were formed at the boundary between the impingement region and the wall jet region. For L/D_e from 2 to 6, the stagnation point Nusselt number varied according to $Nu_s \propto Re^{0.5}$. For a larger nozzle-to-plate distance of $L/D_e = 10$, the Reynolds number dependence was stronger ($Nu_s \propto Re^{0.74}$) due to an increase of turbulence in the approaching jet as a result of the stronger exchange of momentum with the surrounding air. The Nusselt number for the elliptic jet in the impingement region was larger than that for a circular jet. This may be caused by the large entrainment rate and large scale coherent structure of the elliptic jet.

INTRODUCTION

AS AN EFFECTIVE method to enhance heat and mass transfer, impinging jets have been used in a number of applications; this includes the cooling of hot steel plate, the tempering of glass, the drying of papers and films, the cooling of turbine blades, the cooling of electronic components, etc.

Numerous analytical and experimental studies on the heat and mass transfer of impinging jets are found in Hrycak [1], Martin [2], and Downs and James [3]. These studies have dealt with the effects of Reynolds number, nozzle-to-plate distance, nozzle geometry, cross flow, jet orientation, jet temperature, freestream turbulence, etc.

There have been only a few studies that investigated the effects of jet flow structures on the heat transfer enhancement in impinging jets. Kataoka [4] studied the role of artificially-induced large scale eddies in the enhancement of the impinging heat transfer. He correlated the jet impingement heat transfer with turbulence parameters and suggested that the surface renewal effect of large scale turbulent eddies is the dominant mechanism in the heat transfer augmentation at the stagnation point. Gardon and Akfirat [5] investigated the effect of turbulence on the heat transfer augmentation by controlling freestream turbulence with a screen of 18 mesh installed at the slot nozzle.

Popiel and Trass [6] visually studied the flow field of a round impinging jet for small nozzle-to-plate distances where the plate was positioned inside the potential core region. They used a smoke-wire technique and noted ring-shaped wall eddies that were induced between large scale toroidal vortices. Didden and Ho [7] and Walker *et al.* [8] showed that an unsteady boundary separation occurs due to the impingement of ring-shaped vortices on the plate at nozzle-to-plate distances less than the potential core length. Kataoka [4] explains that this is owing to an unsteady adverse pressure gradient in the outer impingement region where the ring-shaped vortices impinge.

Liquid crystals have been used as temperature sensors to measure the heat transfer coefficient in impinging jet heat transfer studies. Hoogendoorn [9] used both a long straight pipe and a smoothly converging nozzle and studied the effects of turbulence on the heat transfer at the stagnation point. Goldstein and Timmer [10] visualized the heat transfer resulting from arrays of impinging jets. Goldstein and Franchett [11] studied the heat transfer to a jet impinging at different oblique angles to a plane surface. Baughn and Shimizu [12], Baughn *et al.* [13], and Yan *et al.* [14] made heat transfer measurements for a fully developed jet impinging on a flat plate. They employed both steady and preheated-wall transient methods and obtained heat transfer coefficients which were in good

NOMENCLATURE

A	area of the gold film Intrex
a	nozzle radius of major axis
b	nozzle radius of minor axis
AR	aspect ratio of elliptic nozzle, a/b
D	pipe diameter
D_e	equivalent diameter of elliptic nozzle, $2\sqrt{(ab)}$
f	gold coating uniformity factor
h	local convective heat transfer coefficient
I	current across the gold film Intrex
k_a	thermal conductivity of air
L	nozzle-to-plate distance
Nu	local Nusselt number, hD_e/k_a
Nu_s	stagnation point Nusselt number
q''_c	convective heat flux
R	radial distance from stagnation point
Re	Reynolds number (based on equivalent diameter, D_e)
T_a	ambient temperature
T_j	jet temperature
T_w	wall temperature of test plate
V	voltage across the gold film Intrex
X	radial distance along the major axis
Y	radial distance along the minor axis.
Greek symbols	
ε	emissivity of liquid crystal surface
σ	Stefan–Boltzmann constant.

agreement with each other. Recently, the use of fast computer and image processing technology has improved an accuracy of temperature measurements that were made with liquid crystals (Akino *et al.* [15], Oh [16], and Lee *et al.* [17]).

Little attention has been given to the effects of nozzle geometry on the impingement heat transfer augmentation. There were few non-circular impinging jet heat transfer studies. Tam and Norum [18] studied supersonic rectangular impinging jets from the acoustics point of view. The elliptic jet has general flow characteristics of axisymmetric jets and plane jets. Depending on the nozzle aspect ratio, it becomes either an axisymmetric jet ($AR = 1$) or plane jet ($AR = \infty$). But the flow characteristics of the elliptic jet having large entrainment and strong mixing are quite different from those of axisymmetric or plane jets. Especially, the spreading rate is larger in the minor axis plane than in the major axis. Consequently, the jet cross-section switches its orientation at some distance downstream from the nozzle (Ho and Gutmark [19], Hussain and Husain [20], and Quinn [21]).

In this study, the local heat transfer coefficients were measured for an air jet issuing from an elliptical nozzle with an aspect ratio of 2.14 that is impinging perpendicularly on a flat plate. The experiments were made for jet Reynolds numbers (based on the equivalent diameter, D_e) of 5000, 10 000, and 20 000 and nozzle-to-plate distances from 2 to 10. Bench mark data with low uncertainties were obtained for well controlled boundary conditions; i.e. a uniform wall heat flux and an ambient jet. A digital image processing system was utilized that yielded an unbiased means for the quantitative color determination of the liquid crystal. No previous studies on the heat transfer of an elliptic impinging jet have been reported.

EXPERIMENTAL APPARATUS

A schematic diagram of the experimental apparatus is shown in Fig. 1. Air supplied from a compressed air storage passes through a filter, pressure regulator, heat exchanger, and flowmeter before entering a long pipe.

The pipe is made of a stainless steel with an internal diameter of 17.8 mm and a length of 124.6 cm (55 diameters). The upstream development length of 55 diameters is long enough to produce a fully developed flow just before an elliptic nozzle. An orifice type elliptic nozzle having an aspect ratio (a/b) of 2.14 is attached at the downstream end of pipe as shown in Fig. 2. The elliptic nozzle has an equivalent diameter of 8.8 mm.

A thermocouple is inserted in a feed-through hole in the pipe 75.4 cm upstream from the end of the nozzle. It is a calibrated 0.25 mm diameter Chromel–Alumel thermocouple, with its junction positioned in the pipe center to measure the jet temperature. Another thermocouple of the same type and gage is placed in the freestream region to measure the ambient temperature. These thermocouples are then connected to an HP-3852A data acquisition system capable of measuring temperatures to an accuracy of ±0.1°C. The entire pipe system is rigidly mounted on the traverse device by which the nozzle-to-plate distance can be adjusted to maximum 20 cm (25 diameters) with an accuracy of 0.05 mm.

The heat exchanger is used to maintain the jet temperature to within ±0.2°C of the ambient temperature. The flow rate is controlled by a check valve and measured with an Omega Engineering precision rotameter capable of measuring the air flow rate to within ±2% of reading.

The test plate is a clear Plexiglas sheet that is 29 cm high, 32.5 cm wide and 1 cm thick. The plate material, Plexiglas, is chosen for its low thermal conductivity which minimizes the heat conduction in the wall. To the surface of the plate is glued a sheet of Intrex (a thin transparent gold film coated on a 0.13 mm polyester sheet substrate). Copper foil strip 'electrodes' are then attached to either end of the surface of the Intrex and silver-loaded paint is applied to

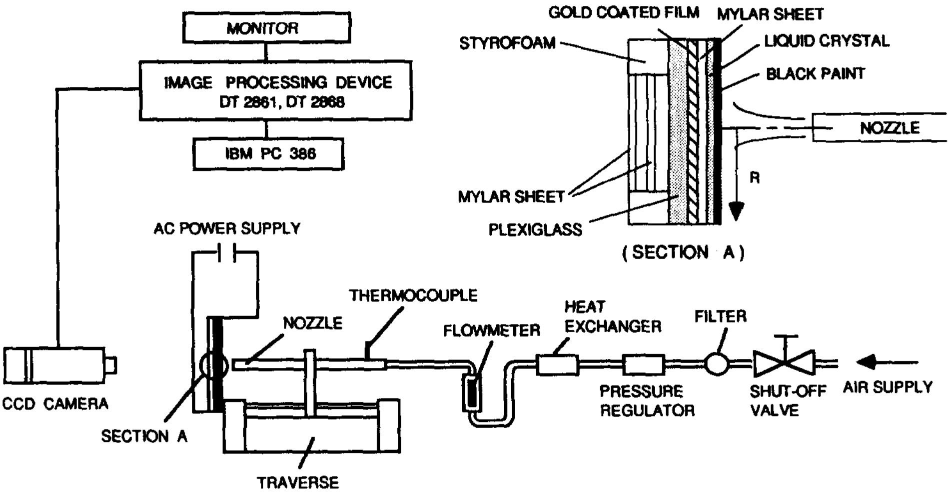

FIG. 1. Schematic diagram of experimental apparatus.

establish a good electrical contact between the copper electrodes and the Intrex surface. By passing an AC current through the Intrex, an essentially uniform wall heat flux boundary condition is created.

The copper electrodes are then connected to a variable transformer in series with a current shunt (rated 50 mV and 5 A), allowing an adjustable AC voltage to be dialed into the electrodes, and the voltage drop across and current input to the Intrex to be measured accurately. Two Fluke 8840A Multimeters are used to measure the voltages across the Intrex and current shunt. A 1 mm thick transparent Mylar sheet is attached to the surface of the gold-coated Intrex to prevent a chemical reaction between the gold and liquid crystal. An air brush is used to uniformly apply first a thin layer of liquid crystal and then black backing paint. The combined thickness of liquid crystal and paint is about 0.05 mm.

To minimize the conduction heat losses, 1 mm thick Mylar sheets are placed behind the test plate creating air gaps between the Mylar sheets and between the test plate and an adjoining Mylar sheet (see Fig. 1). The entire plate assembly is mounted vertically with the test surface perpendicular to the direction of the jet flow. All of the layers behind the liquid crystal are transparent and the liquid crystal colors are viewed from the rear of the test plate.

The liquid crystal used in this experiment is 'R35C1W' micro-encapsulated thermochromic liquid crystal purchased from Hallcrest Liquid Crystal Technology, Illinois. This liquid crystal has a narrow band of approximately 1°C over which the entire color spec-

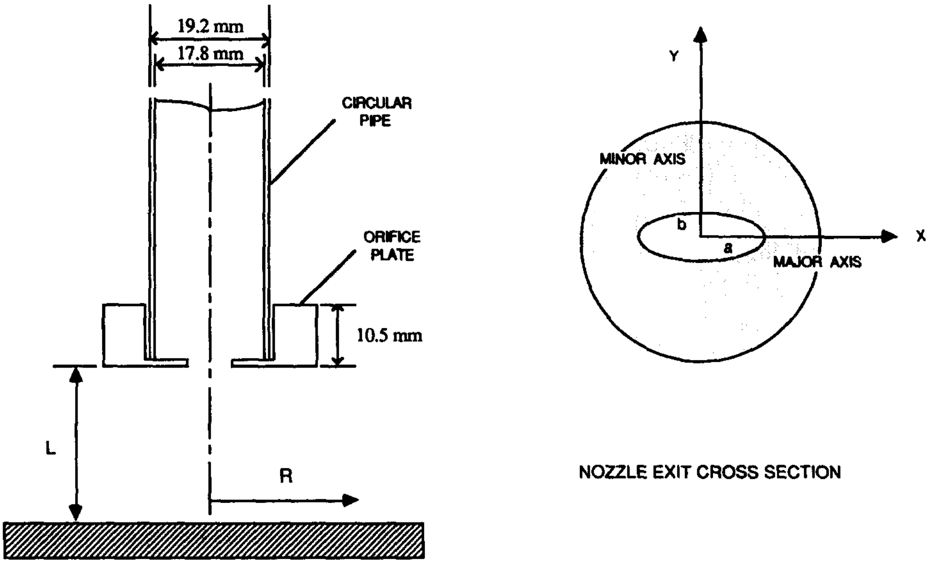

FIG. 2. Elliptic nozzle and coordinate system.

trum occurs (the color red nominally starting at 35°C and the color blue starting at 35.8°C). The black backing paint 'BB-G1' compatible with this liquid crystal was also purchased from Hallcrest.

In order to accurately determine the spatial location of a specified isotherm and to minimize any visual bias, a digital image processing system has been used. The isotherms of the yellow-to-red transition band (the liquid crystal is calibrated at the change of the red color from yellow which is 35.2 ± 0.15°C) are obtained with a red color filter using a high sensitivity Panasonic WV-BL600 CCD camera, digitized with a Data Translation DT-2861 frame grabber, and processed with an IBM-PC/386 and a high speed DT-2868 frame processor. Detailed information on the image processing system and liquid crystal calibration are given in Lee *et al.* [17].

DATA REDUCTION

The heated gold film Intrex-liquid crystal technique used in this study provides a nearly uniform wall heat flux boundary condition with less than 1% conduction loss to the Plexiglas plate (Baughn *et al.* [22]) to which the Intrex is attached, and a method to determine the surface isotherms using liquid crystals. The heat flux can be adjusted by changing the electrical current through the Intrex, which changes the surface temperature. Because of the constant heat flux condition, an isotherm on the Intrex surface also corresponds to a contour of a constant heat transfer coefficient. As the heat flux changes, the position of the color isotherm is also moved. The local convective heat transfer coefficient at the position of the particular color being observed is calculated from

$$h = q_c''/(T_w - T_j) \tag{1}$$

where, q_c'' is obtained by subtracting the energy loss from the total heat flux through the Intrex and given by:

$$q_c'' = fIV/A - \varepsilon\sigma(T_w^4 - T_a^4). \tag{2}$$

Here, f is the ratio of the local electrical heating to the average heating and is a measure of the uniformity in the gold coating on the Intrex. Baughn *et al.* [22, 23] evaluated and found the uniformity to be as high as 98% for a carefully selected small size of the Intrex corresponding to the present experiment. Therefore, we assume $f \approx 1$ for the heat flux calculation, but f is maintained in equation (2) because it contributes to the uncertainty (see Table 1). The emissivity, ε, for the liquid crystal coated on the plate surface was measured and found to be 0.5 with an uncertainty of 0.05 in Hechanova [24].

The uncertainty in the local Nusselt numbers has been estimated using methods suggested by Kline and McKlintock [25] with a 95% confidence level. It is shown in Table 1 that the overall uncertainty in the Nusselt number is estimated as 3.14%. The individual contributions of each measured variable to the overall uncertainty are also shown in the Table for specified conditions. Note that the uncertainty in the gold coating uniformity factor, f, is the largest contribution to the overall uncertainty. Another important source of uncertainty is the liquid crystal measurement of the plate wall temperature, T_w. The uncertainty in the Reynolds number is estimated to be 2.5%. The uncertainty in the position (R/D_e) along the plate is estimated to be 1.0%.

RESULTS AND DISCUSSION

The time-averaged heat transfer along the impinging surface was obtained for the four dimensionless nozzle-to-plate distances of $L/D_e = 2$, 4, 6, and 10. The results are expressed as the Nusselt number, Nu, vs dimensionless radial distance, R/D_e, in Figs. 3–7. The Reynolds numbers (based on an equivalent nozzle diameter, D_e) used are 5000, 10 000, and 20 000. In these Figures, hollow symbols indicate the Nusselt number along the major axis and solid symbols are along the minor axis. In general, the results show the maximum heat transfer at or near the central stagnation point with monotonically decreasing curves for large nozzle-to-plate distances and curves with a second or third maximum for small nozzle-to-plate distances. The values of the Nusselt number increase as the jet Reynolds number increases.

The Nusselt number distributions for $L/D_e = 2$ are shown in Fig. 3. A cross-over (axis-switching) of the Nusselt number curves along the major and minor

Table 1. Nusselt number uncertainty analysis (at $(L/D_e) = 10$, $(R/D_e) = 1.5$ (major axis), $Re = 20\,000$)

x_i	Value	δx_i	$[(\delta x_i/Nu)(\partial Nu/\partial x_i)] \times 100(\%)$
f	1.0	0.02	2.06
T_w	35.2 (°C)	0.15	1.82
T_j	26.71 (°C)	0.10	1.21
D	8.8 (mm)	0.05	0.58
A	0.0492 (m^2)	0.000246	0.51
I	1.851 (A)	0.00585	0.33
V	55.26 (V)	0.17	0.31
ε	0.5	0.05	0.13
Total Nu uncertainty: $\delta Nu/Nu = 3.14\%$			

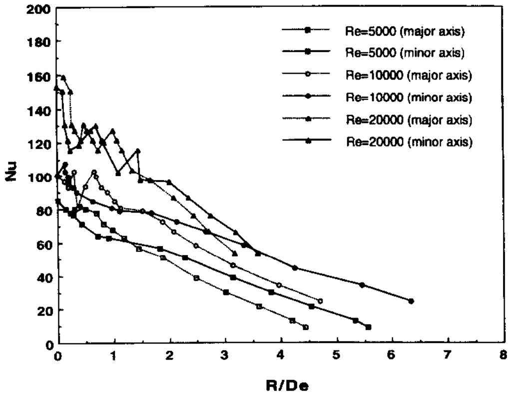

FIG. 3. Radial Nusselt number distribution for $L/D_e = 2$.

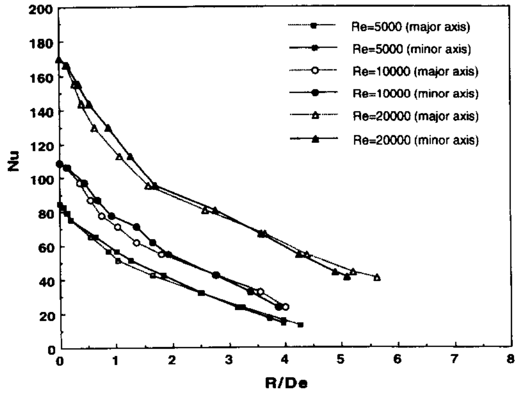

FIG. 5. Radial Nusselt number distribution for $L/D_e = 6$.

axis occurs at $R/D_e \cong 1.5$ for all Reynolds numbers tested. This cross-over point is associated with a transition from the stagnation region to the wall jet region. Ho and Gutmark [19] found in their fluid mechanics studies with an elliptic nozzle having an aspect ratio of 2 that the axis-switching occurs due to a difference in the spreading rate along the major and minor axes. Along the minor axis the elliptic jet spreads out widely into the ambient fluid, while in the major axis plane the shear layer shrinks in the jet center in the near field. In the region corresponding to $R/D_e > 1.5$, the Nusselt number profiles along the minor axis show higher values than those along the major axis. But for $0.5 < R/D_e < 1.5$, the Nusselt number values are smaller along the minor axis.

Figure 3 is for the shortest nozzle-to-plate distance tested ($L/D_e = 2$). For this distance the plate is within the potential core length of the jet and the heat transfer variation is very complicated due to the complex interactions between the impinging jet and the plate. For $Re = 10\,000$ and $20\,000$, there are three maxima in the Nusselt number. One maximum occurs at the stagnation point, and second and third maxima result from toroidal vortices formed on the impingement surface between the stagnation region and the wall jet region. When the elliptic jet impinges upon the plate, two strong toroidal vortices are induced from the asymmetric azimuthal vortex structure of the elliptic jet, resulting in the second and third peaks in the heat transfer coefficients (see Fig. 11(a)). Figure 11 will be discussed later.

Figure 4 shows the Nusselt number profiles at $L/D_e = 4$. The heat transfer behaviors for all three Reynolds numbers are nearly identical both in the major and minor axis planes: monotonically decreasing curves along the impingement surface. It should be noted that the axis-switching occurs at $R/D_e \cong 2$ for all Reynolds numbers tested.

The radial Nusselt number profiles for $L/D_e = 6$ and 10 are shown in Figs. 5 and 6, respectively. These profiles show a monotonic decrease in the Nusselt number as R/D_e increases. It is reported in refs. [12, 17] that for the round impinging jet, the maximum stagnation point heat transfer was obtained when the plate is placed near $L/D_e = 6$. But in this study the heat transfer at the stagnation point for $L/D_e = 6$ and for $Re = 5000$ and $10\,000$ is smaller than for $L/D_e = 2$ and 4. This results from the fact that the elliptic jet has a shorter potential core length and a higher spreading rate than the round impinging jet (see Fig. 17 of Ho and Gutmark [19]). For $L/D_e = 6$, ambient fluids are entrained up to the elliptic jet centerline and large momentum loss would occur before the jet impinges upon the heat transfer surface.

Figure 7 is plotted to investigate the heat transfer behaviors for $Re = 20\,000$. It is shown that the axis-

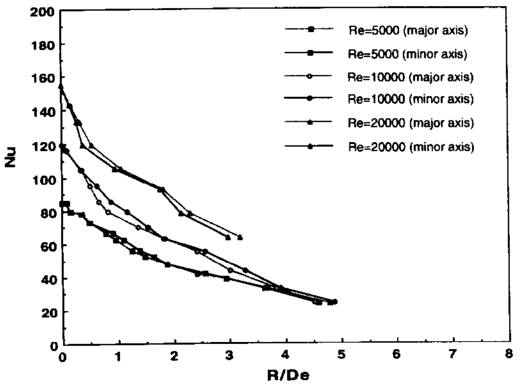

FIG. 4. Radial Nusselt number distribution for $L/D_e = 4$.

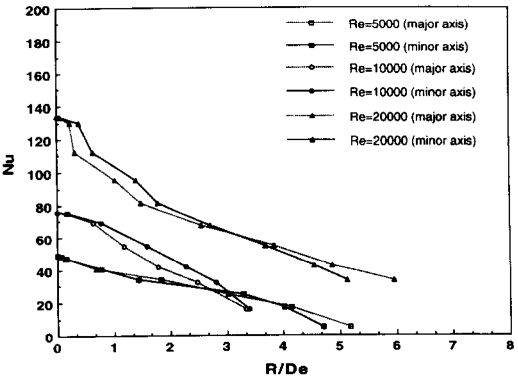

FIG. 6. Radial Nusselt number distribution for $L/D_e = 10$.

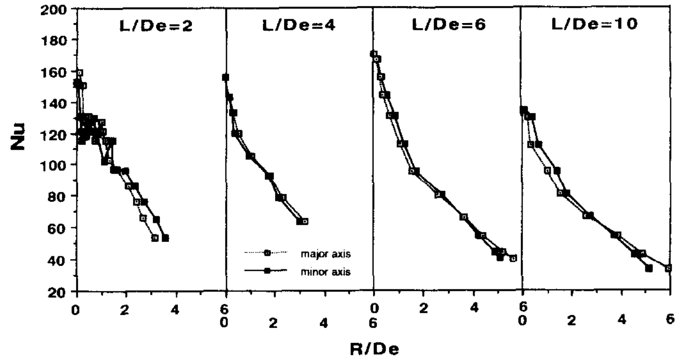

FIG. 7. Nusselt number distribution at $L/D_e = 2, 4, 6$, and 10 for $Re = 20\,000$.

switching position shifts downstream from $R/D_e \cong 1.5$ to 3 as L/D_e increases. Note that for all L/D_e except $L/D_e = 2$, the Nusselt number values are higher in the major axis than in the minor axis after the axis-switching.

Figure 8 shows the Nusselt number distributions for an elliptic impinging jet for $L/D_e = 10$ and $Re = 20\,000$ compared with those of a round impinging jet by Goldstein and Franchett [11]. The heat transfer coefficient for the elliptic jet at the stagnation point is about 10% higher than for the round jet, but falls rapidly to match the round jet and becomes slightly less in the region corresponding to $R/D_e \geqslant 5$. According to Ho and Gutmark [19], the higher heat transfer for the elliptic jet at the stagnation region than the round jet is due to the self-induction of the large scale asymmetric coherent structure of the elliptic jet that causes azimuthal distortions of the elliptic vortex ring, and thereby the large entrainment of the surrounding fluid in to the jet.

Figure 9 shows the effect of the nozzle-to-plate distance on the stagnation point heat transfer. For $Re = 20\,000$, the maximum stagnation point heat transfer occurs at $L/D_e \cong 6$. But, for the smaller Reynolds numbers, the maximum occurs at $L/D_e \cong 4$, which is a shorter distance than for the round impinging jet, due to a shorter length of the jet potential core.

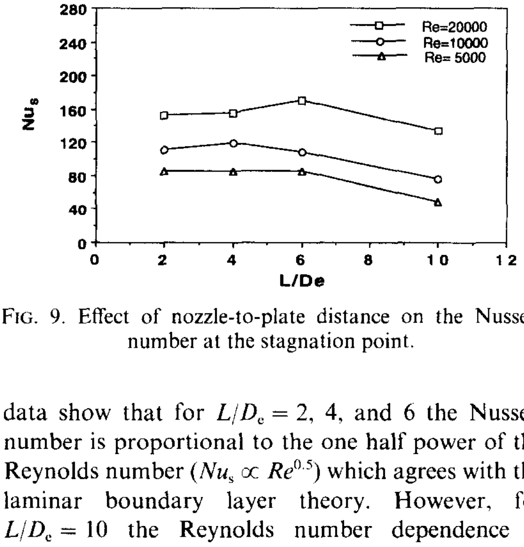

FIG. 9. Effect of nozzle-to-plate distance on the Nusselt number at the stagnation point.

The dependency of the stagnation point Nusselt number on Reynolds number is shown in Fig. 10. The data show that for $L/D_e = 2$, 4, and 6 the Nusselt number is proportional to the one half power of the Reynolds number ($Nu_s \propto Re^{0.5}$) which agrees with the laminar boundary layer theory. However, for $L/D_e = 10$ the Reynolds number dependence is stronger ($Nu_s \propto Re^{0.74}$). This is attributed to an increase of turbulence in the approaching jet (see Figs. 18 and 19 of Ho and Gutmark [19]). This is a result of the stronger exchange of momentum with the surrounding air, which increases the transport in the otherwise laminar boundary layer in the stagnation region. Lee *et al.* [17] and Yan *et al.* [14] have reported similar behavior for the round impinging jet for which the exponents varied from 0.52 to 0.7 depending on the nozzle-to-plate distance and Reynolds number tested.

Figure 11 shows the shapes of isothermal contours

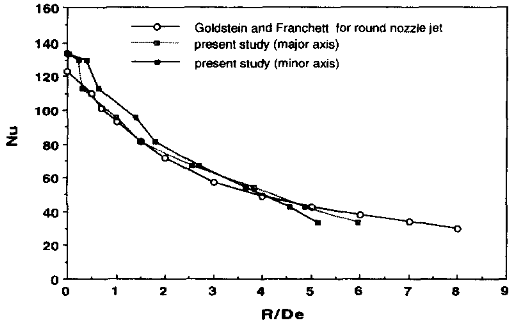

FIG. 8. Nusselt number distribution for an elliptic jet compared with a round jet at $L/D_e = 10$ for $Re = 20\,000$.

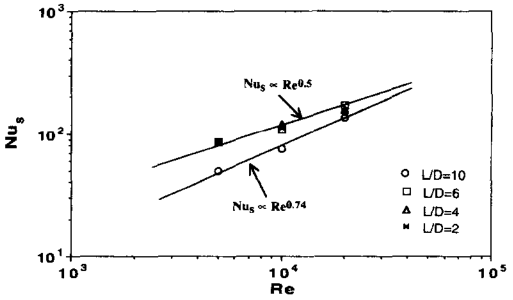

FIG. 10. Correlation between the stagnation point Nusselt number and Reynolds number.

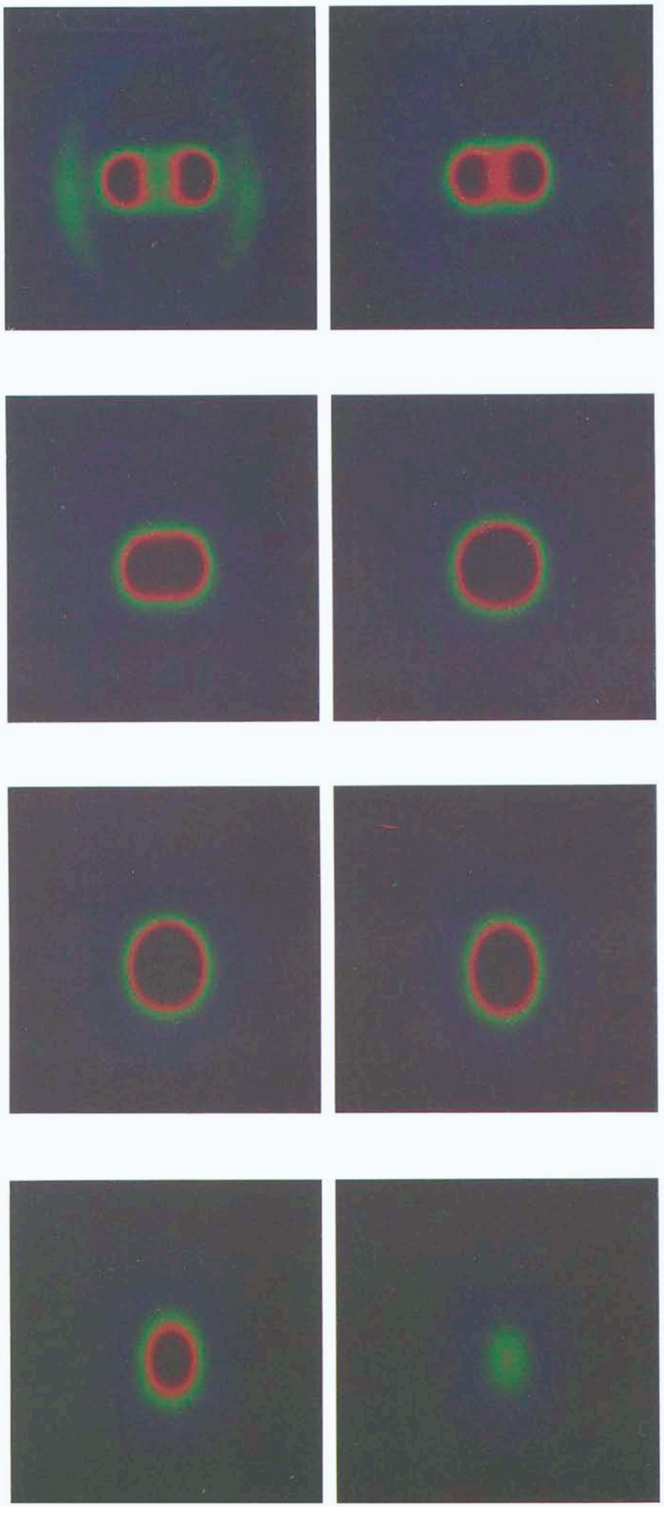

on the impingement surface for $Re = 20\,000$, $q''_c = 3080$ W m^{-2}, and L/D_e from 2 to 10. At small $L/D_e (\leqslant 3)$, there exist two secondary jets at the major axis which probably result from the self-induction velocity of the vortex structure of the elliptic jet. The two jets are then merged into the elliptic shape at $L/D_e \cong 4$ that has the same elliptical orientation as the nozzle. As the L/D_e increases, the elliptic cross-section switches its orientation, resulting in the near-circle shape at $L/D_e \cong 5$ and the elliptic shape with the opposite orientation as the nozzle at $L/D_e \geqslant 6$. This occurs due to a larger spreading rate in the minor axis plane than in the major axis plane. Beyond $L/D_e = 10$, the elliptic jet loses much of its momentum before arriving at the impingement surface (see Fig. 11(h)). The constant velocity contours (see Fig. 16 of Ho and Gutmark [19]) and flow visualization study (see Fig. 5 of Hussain and Husain [20]) that investigated the deformation of vortical structures in the 2 : 1 elliptic jet show similar changes in the shape of the jet cross-section at various positions downstream from the nozzle. Ho and Gutmark [19] also reported that the axis-switching occurred three times in the range of $L/a \leqslant 40$ (where, a is the nozzle radius of the major axis).

CONCLUSIONS

This experimental study was carried out to investigate the local heat transfer characteristics of an elliptic impinging jet issuing from an elliptic slot nozzle of aspect ratio of 2.14. For $L/D_e = 2$ and for $Re = 10\,000$ and $20\,000$, the local Nusselt number distributions exhibit a non-monotonic variation with second and third maxima in the Nusselt number occurring. All the other cases exhibit monotonically decreasing values of the Nusselt number. The second and third maxima result from the induced toroidal vorticies that are formed on the impingement surface between the stagnation regon and wall jet region.

The maximum stagnation point heat transfer for the elliptic jet occurs at a shorter nozzle-to-plate distance than for the round impinging jet due to a shorter length of the potential core for the ellipitic jet. The Nusselt numbers at the stagnation point are well correlated by Re^n. For $L/D_e = 2$, 4, and 6, n is 0.5. For $L/D_e = 10$, n is 0.74.

The isothermal contour on the uniformly heated plate changed in shape from elliptic to near circle to elliptic again with increasing R/D_e as the elliptical cross-section switched its orientation. The elliptic jet yields Nusselt numbers at the stagnation region that are higher at $Re = 20\,000$ and for $L/D_e = 10$ than for the round jet due to the large entrainment of the surrounding fluid.

Acknowledgements—The authors wish to express their appreciation to the Pohang Institute of Science and Technology, Advanced Fluids Engineering Research Center for the support of this project. One of the authors (D. Lee) gratefully acknowledges the hospitality offered by the Pohang Institute of Science and Technology in Korea during his stay in 1992. Many valuable comments by Professor Ralph Greif at the University of California, Berkeley are also gratefully acknowledged.

REFERENCES

1. P. Hrycak, Heat transfer from round impinging jets to a flat plate, *Int. J. Heat Mass Transfer* **26,** 1857–1865 (1983).
2. H. Martin, Heat and mass transfer between impinging gas jets and solid surfaces. In *Advances in Heat Transfer*, Vol. 13, pp. 1–60. Academic Press, New York (1977).
3. S. J. Downs and E. H. James, Jet impingement heat transfer—a literature survey, ASME Paper 87-HT-35, New York (1987).
4. K. Kataoka, Impingement heat transfer augmentation due to large scale eddies, *Proc. 9th Int. Heat Transfer Conf.*, Vol. 1, pp. 255–273 (1990).
5. R. Gardon and J. C. Akfirat, The role of turbulence in determining the heat transfer characteristics of impinging jets, *Int. J. Heat Mass Transfer* **8,** 1261–1272 (1965).
6. C. O. Popiel and O. Trass, Visualization of a free and impinging round jet, *Exp. Thermal Fluid Sci.* **4,** 253–264 (1991).
7. N. Didden and C. M. Ho, Unsteady separation in a boundary layer produced by an impinging jet, *J. Fluid Mech.* **160,** 235–256 (1985).
8. J. D. A. Walker, C. R. Smith, A. W. Cerra and T. L. Doligalki, The impact of a vortex ring on a wall, *J. Fluid Mech.* **181,** 99–140 (1987).
9. C. J. Hoogendoorn, The effect of turbulence on heat transfer at stagnation point, *Int. J. Heat Mass Transfer* **20,** 1333–1338 (1977).
10. R. J. Goldstein and J. F. Timmer, Visualization of heat transfer from arrays of impinging jets, *Int. J. Heat Mass Transfer* **125,** 1857–1868 (1982).
11. R. J. Goldstein and M. E. Franchett, Heat transfer from a flat surface to an oblique impinging jet, *Trans. ASME J. Heat Transfer* **110,** 84–90 (1988).
12. J. W. Baughn and S. Shimizu, Heat transfer measurement from a surface with uniform heat flux and an impinging jet, *Trans. ASME J. Heat Transfer* **111,** 1096–1098 (1989).
13. J. W. Baughn, T. E. Hechanova and X. Yan, An experimental study on entrainment effects on the heat transfer from a flat surface to a heated circular impinging jet, *Trans. ASME J. Heat Transfer* **113,** 1023–1025 (1991).
14. X. Yan, J. W. Baughn and M. Mesbah, The effect of Reynolds number on the heat transfer distribution from a flat plate to an impinging jet, *ASME Winter Annual Meeting*, Anaheim, CA (1992).
15. N. Akino, T. Kunugi, K. Ichimaya, K. Mitsushiro and M. Ueda, Improved liquid crystal thermometry excluding human color sensation, *Trans. ASME J. Heat Transfer* **112,** 558–565 (1989).
16. S. M. Oh, An experimental study of heat transfer on a heated flat plate by a circular impinging jet, M.S. Thesis, Pohang Institute of Science and Technology, Korea (1992).
17. S. J. Lee, J. H. Lee, D. Lee and R. Greif, Heat transfer from a plate to a fully developed axisymmetric impinging jet, *ASME Winter Annual Meeting*, New Orleans, LA (1993).
18. C. K. W. Tam and T. D. Norum, Impingement tones of large aspect ratio subsonic rectangular jets, *AIAA J.* **30,** 304–311 (1992).
19. C. M. Ho and J. Gutmark, Vortex induction and mass entrainment in a small aspect ratio elliptic jet, *J. Fluid Mech.* **179,** 383–405 (1987).
20. F. Hussain and H. S. Husain, Elliptic jets, Part 1.

Characteristics of unexcited and exited jets, *J. Fluid Mech.* **208,** 257–320 (1989).

21. W. R. Quinn, On mixing in an elliptic turbulence free jet, *Phys. Fluids* **1,** 1716–1722 (1989).
22. J. W. Baughn, M. A. Hoffman, R. K. Takahashi and B. E. Launder, Local heat transfer downstream of an abrupt expansion in a circular channel with constant wall heat flux, *Trans. ASME J. Heat Transfer* **106,** 789–796 (1984).
23. J. W. Baughn, P. T. Ireland, T. V. Jones and N. Saniei, A comparison of the transient and heated-coating methods for the measurements of the local heat transfer coefficients on a pin fin, *Trans. ASME J. Heat Transfer* **111,** 877–881 (1989).
24. T. E. Hechanova, An experimental study of entrainment effects on heat transfer from a surface with a fully developed impinging jet, M. S. Thesis, University of California, Davis (1986).
25. S. J. Kline and F. A. McKlintock, Describing uncertainties in single sample experiments, *Mech. Engng.* **75,** 3–8 (1953).